



HAL
open science

Multipactor Thresholds Prediction for Geometries Subject to Standing Waves

Eva Al Hajj Sleiman, Julien Hillairet, Mohamed Belhaj

► **To cite this version:**

Eva Al Hajj Sleiman, Julien Hillairet, Mohamed Belhaj. Multipactor Thresholds Prediction for Geometries Subject to Standing Waves. *IEEE Transactions on Plasma Science*, 2024, 52 (3), pp.938 - 950. 10.1109/tps.2024.3372192 . hal-04664655

HAL Id: hal-04664655

<https://hal.science/hal-04664655>

Submitted on 30 Jul 2024

HAL is a multi-disciplinary open access archive for the deposit and dissemination of scientific research documents, whether they are published or not. The documents may come from teaching and research institutions in France or abroad, or from public or private research centers.

L'archive ouverte pluridisciplinaire **HAL**, est destinée au dépôt et à la diffusion de documents scientifiques de niveau recherche, publiés ou non, émanant des établissements d'enseignement et de recherche français ou étrangers, des laboratoires publics ou privés.

Multipactor Thresholds Prediction for Geometries Subject to Standing Waves

Eva Al Hajj Sleiman¹, Julien Hillairet², and Mohamed Belhaj³

Abstract— High-power radio frequency (RF) systems, such as those found in high-voltage/current test beds for RF component testing and RF plasma heating antennas, often experience standing waves (SWs). In such scenarios, the amplitude of electromagnetic (EM) fields ceases to be longitudinally homogeneous, and the resulting electric field gradient nonlinearly influences electron trajectories, introducing challenges in predicting multipactor, the exponential electron-growth mechanism, compared to traveling wave (TW) cases. This study identifies a specific regime where the mean and maximum electric field magnitudes characterize the upper and lower multipactor thresholds independently of the reflection coefficient. This unique regime enables the prediction of multipactor thresholds in devices using simulations with a single, forward-TW, eliminating the need for extensive simulations involving multiple waves' excitation. Unlike previous works focusing solely on predicting thresholds initiating multipactor in geometries subject to SWs, our interest extends to predicting the upper multipactor thresholds, beyond which electron-growth diminishes. We use the commercial software Spark-3D, employed as a breakdown analysis tool, to determine the lower and upper multipactor scaling factors for complex 3-D geometries subject to SWs. By comparing multipactor electric fields for SW cases to those for TW cases, we propose multipactor electric field thresholds that remain constant independently of the reflection coefficient within the frequency range of interest.

Index Terms— Coaxial transmission line, high power, multipactor, radio frequency (RF), resonator, standing wave (SW), total electron emission yield (TEEY).

I. INTRODUCTION

MULTIPACTOR is a vacuum discharge observed in microwave structures [2] at sufficiently low pressures so that the electron-free path is longer than the vacuum space [3]. The multipactor mechanism sustains itself by secondary electron emission, resulting from electrons' impact on the component surfaces. Multipactor can be observed in many applications, such as space applications, in particular,

Manuscript received 15 June 2023; revised 5 January 2024; accepted 25 February 2024. Date of publication 13 March 2024; date of current version 22 May 2024. This work was supported by the European Union through the Euratom Research and Training Programme within the Framework of the EUROfusion Consortium under Grant 101052200—EUROfusion. The review of this article was arranged by Senior Editor S. J. Gitomer. (Corresponding author: Eva Al Hajj Sleiman.)

Eva Al Hajj Sleiman is with CEA, IRFM, 13108 Saint-Paul-lez-Durance, France, and also with ONERA, DPHY, Université de Toulouse, 31055 Toulouse, France (e-mail: eva.alhajjsleiman@cea.fr).

Julien Hillairet is with CEA, IRFM, 13108 Saint-Paul-lez-Durance, France.

Mohamed Belhaj is with ONERA, DPHY, Université de Toulouse, 31055 Toulouse, France.

Color versions of one or more figures in this article are available at <https://doi.org/10.1109/TPS.2024.3372192>.

Digital Object Identifier 10.1109/TPS.2024.3372192

radio frequency (RF) satellite payloads [13]; experimental tokamak RF components: antennas, transmission lines, and RF windows [15]; and microwave vacuum tubes [16] or particle accelerator structures [14].

For multipactor to occur in all-metal devices, two conditions must be simultaneously fulfilled [4]: 1) one necessary but not sufficient condition that the impact energy of electrons colliding with an electrode must be sufficient so that the total electron emission yield (TEEY) of the electrode surface is greater than one and 2) the second condition is the resonance condition for the electron's motion to be synchronized with the phase change of the RF electric field.

Contrary to signal amplification applications where the multipactor is beneficent, we are particularly interested in applications where the consequences of multipactor are problematic and may affect or limit the performance of the RF components [5]. As multipactor experiments are expensive, especially with complex big dimensions components and for a megawatt range of RF power, we rely on numerical tools for multipactor predictions.

TITAN [1] is a test-bed facility devoted to ion cyclotron resonance heating (ICRH) subassembly testing, built at CEA-Cadarache in France. Within this test-bed facility, the under-test component is connected to a high-power RF generator, delivering up to 2 MW in the frequency range 46–65 MHz. An RF resonator was used to reach relevant RF performance under vacuum conditions, i.e., a voltage in the order of a few tens of kilovolts and current in the range of thousands of amperes. This resonator was made of two coaxial transmission lines fed with a T-junction. One of these branches is connected to the device under test, followed by a variable-matching short circuit. The other one is also connected to a variable-matching short circuit. For a given generator's frequency, the matching point is achieved by optimizing the electric lengths of the coaxial transmission lines, being the two variable-matching components. This resonator operated at levels up to (50 kV–3 kA) to mimic the operating voltage and current of the devices under test (for a single frequency) [18]. The resonator is fed by an RF generator with a 30- Ω coaxial transmission line. Being an under-vacuum device, it is therefore prone to multipactor.

In such applications, RF components are tested at high voltage (or current) densities in ranges that can be above the upper multipactor thresholds. Therefore, in practice, the multipactor power bands of the different parts of the resonator are bypassed during operation. However, it requires ramping

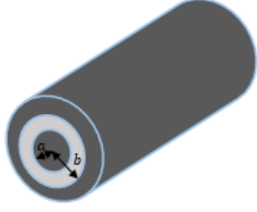


Fig. 1. Coaxial transmission line geometry's representation. The light gray represents the vacuum and the dark gray represents the conductors. The inner and outer conductors are, respectively, of radii a and b .

up the RF power sufficiently fast to minimize the time spent in the multipactor regions to avoid multipactor to develop and detune the RF system [5]. This operation elucidates the necessity for determining the lower and the upper multipactor thresholds of all the resonator's parts.

Contrary to other applications where the RF components are matched to the load, preventing reflected power from flowing back to the source, the main specificity of the double-branch resonator is its operation with a high standing wave ratio (SWR). In this case, the wave pattern is the superposition of an incident and reflected waves. The benefit of the resonator's operation under standing waves (SWs) is that we can achieve high voltages or currents at specific target locations within the resonator branches with relatively low input power. Nevertheless, the remaining components of the resonator are subject to low voltages or currents. Since the voltage gradient affects the electrons' trajectories, it is crucial to determine the lower and upper multipactor thresholds for SW cases and to determine relevant multipactor quantities for these multipactor thresholds regardless of the reflection coefficient values.

This article aims to identify a regime where the lower and the upper (when existing) multipactor thresholds are constant, regardless of the amount of reflected power. Two geometries are considered herein: 1) a coaxial transmission line of characteristic impedance $50\ \Omega$ analyzed in the frequency range [25, 1500] MHz and 2) the different parts of the resonator of the TITAN test-bed facility at a frequency of 63 MHz.

The rest of this article is organized as follows. Section II lists the previous findings on the multipactor thresholds' determination in SW regimes. Section III presents the geometries models analyzed here. Section IV explains the generic methodology applied to determine the relevant quantities for the lower and upper multipactor thresholds, regardless of the percentage of the reflected power. The obtained results are detailed in Section V. Finally, Section VI concludes the work.

II. PREVIOUS FINDINGS

Somersalo et al. [6] applied a computational method on quarter-wavelength coaxial transmission lines operating under traveling wave (TW), mixed wave (MW), and SW. The coaxial transmission line is excited only from one side. Hence, the multipactor power threshold is defined as incident power. They used their developed method to determine the multipactor power thresholds, type, and order; by following the electron trajectories in the structures.

They found that, for SW, the surviving trajectories, being the electrons causing multipactor, are the ones that appear near the maximum of the electric field. Moreover, they stated that the contribution of the surviving electrons far from the electric field's maximum appeared at higher incident powers, and the nonphase focusing electrons far from the electric field's maximum drift toward the minimum of the electric field as the power increases. They deduced that the multipactor for coaxial transmission lines operating in SW is due to the electric field within their power-incident range. In addition, they proposed a scaling law relating the multipactor powers of the TW case to those of the SW case. This scaling law is given by $P_{TW} = 4P_{SW}$ since the peak voltage of the SW is twice that of the TW in such a case.

For the MW case, they found that when the reflection coefficient is higher than zero (TW case), the multipactor resonance regime splits into two distinct modes. The first set of resonance modes will coincide with the *electric* multipactor mode of the SW case. The second set, caused by the magnetic field, shifts to very high incident powers and is known as the *magnetic* multipactor mode. A scaling law exists between the electric multipactor powers of the MW case and the TW multipactor powers and is given by $P_{MW} \sim (1/(1+R)^2)P_{TW}$. They summarized that the multipactor for the TW case is of mixed nature, where both the electric and magnetic fields contribute to the multipactor. However, as the reflection coefficient increases, the multipactor processes are dissociated into electric and magnetic multipactor processes, whereas for the pure SW case, the multipactor resonance mode appears close to the maximum of the electric field, and no multipactor is maintained at the electric field nodes. Somersalo et al. [6] indicate that the *magnetic* multipactor process does not exist for this case since it requires infinite incident power for it to be sustained. However, some missing multipactor processes have not been considered due to numerical limitations, and the scanned incident power range is limited to hundreds of kilowatts.

Perez et al. [9] have developed a numerical model to predict the multipactor thresholds for coaxial transmission lines of infinite length in the propagation direction. Here, the authors choose to excite the coaxial transmission line from both ports so that the resultant wave is a superposition of two waves propagating in opposite directions. These transmission lines are subject to three types of RF signals of different reflection coefficients: 1) TW corresponding to a null reflection; 2) MW defined by a 50% reflection coefficient; and 3) SW corresponding to a 100% reflection. Their model was based on the computation of effective electron trajectories perturbed by the electromagnetic (EM) fields and the inter-electron interactions to account for the space charge effect due to Coulombian repulsion. They have focused only on the lower voltage multipactor thresholds and have found that the voltage multipactor thresholds are higher for the SW case than the case of a TW for high values of $f \times d$ products (where f is the frequency and d is the distance separating the inner conductor from the outer one). They attributed this effect to low electric field regions' existence in the wave propagation direction (SW nodes), absorbing the electrons before the multipactor

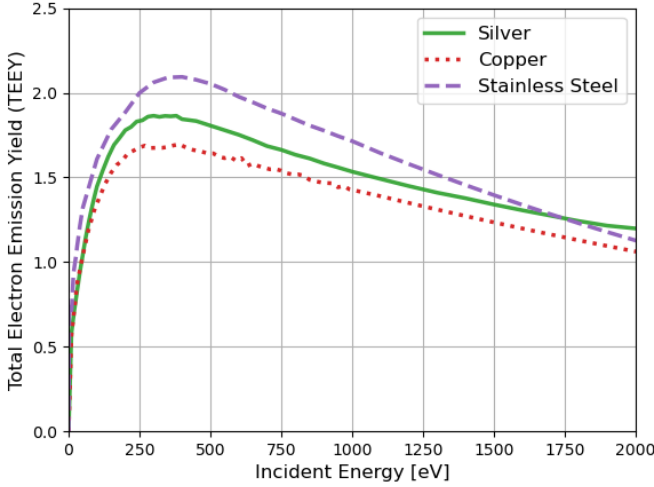


Fig. 2. TEEY data for silver-coated, copper, and stainless steel samples.

phenomenon ignition. They found that this effect is more pronounced for $f \times d$ products higher than $700 \text{ MHz} \cdot \text{cm}$, independently of the choice of f and d and the chosen material. Nevertheless, for $f \times d$ products less than this barrier, the voltage multipactor thresholds are the same for SW, MW, and TW cases.

Romanov [10] performed simulations of multipactor discharge using CST Particle Studio for a coaxial transmission line subject to SW. The findings of Perez et al. [9] were confirmed to come from the Gaponov–Miller force (also known as ponderomotive force) that pushes electrons toward the low electric field region and contributes to mitigating multipactor. In addition, three multipactor zones have been identified in the SW mode: 1) the low electric field zones showing the similarity between the multipactor for SW and that for TW, where the ponderomotive force has, yet no effect; 2) a medium electric field zone where this force gains strength and secondary electrons are more concentrated in the electric field nodes; and 3) the high electric field zones where the concentration of electrons is denser on a small volume located in the electric field nodes. The results from Romanov’s work [10] disagreed with the analysis done by Somersalo et al. [6] for the SW case since their simulations have shown multipactor near the nodes of the electric field.

III. INVESTIGATED GEOMETRIES

Two geometries are elaborated: 1) a $50\text{-}\Omega$ coaxial transmission line of stainless steel silver-coated material and 2) the resonator of the TITAN test-bed facility, constituted of three different material types: silver, copper, and stainless steel. The TEEYs used for the different materials are measured at ONERA/DPHY [20] and are given in Fig. 2.

A. Coaxial Transmission Line

We consider a uniform coaxial transmission line consisting of an inner conductor of radius a and an outer conductor of radius b , where $d = b - a$ ($d = 4 \text{ cm}$) is the gap spacing between electrodes (illustrated in Fig. 1). At each frequency f , the length of the coaxial transmission line in

the propagation direction is $\lambda/2$, λ being the wavelength corresponding to the frequency f . The RF EM fields are described by a superposition of two TEM waves traveling in opposite directions ($+z$ and $-z$), i.e., both ports are excited, respectively, with $p\angle\psi$ and $R^2p\angle\psi$. p and R^2p are the incident powers on the first and second ports, respectively. R and ψ are, respectively, the magnitude and phase of the reflection coefficient $\Gamma = Re^{j\psi}$. The total incident powers on both ports are normalized to 1 W , leading to $p = (1/1 + R^2)$. Three cases will be considered: 1) TW, expressed by $R = 0$; 2) MW, expressed by $0 < R < 1$, and $\psi = 0^\circ$ (particularly we are interested in the case $R = 0.5$); and 3) SW, given by $R = 1$ and $\psi = 0^\circ$. Hence, we can express the RF fields by

$$\vec{E}(\vec{r}, t) = \frac{V}{\sqrt{1 + R^2 r \ln(\frac{b}{a})}} \cos(\omega t - \beta z) \vec{e}_r + \frac{RV}{\sqrt{1 + R^2 r \ln(\frac{b}{a})}} \cos(\omega t + \beta z + \psi) \vec{e}_r \quad (1)$$

$$\vec{B}(\vec{r}, t) = \frac{V}{\sqrt{1 + R^2 c r \ln(\frac{b}{a})}} \cos(\omega t - \beta z) \vec{e}_\varphi - \frac{RV}{\sqrt{1 + R^2 c r \ln(\frac{b}{a})}} \cos(\omega t + \beta z + \psi) \vec{e}_\varphi \quad (2)$$

where $(\vec{e}_r, \vec{e}_\varphi, \vec{e}_z)$ are the unit vectors of the cylindrical coordinates (r, φ, z) , \vec{r} is the position vector, c is the light speed, $V = V_{1W} = (2Z_0)^{1/2}$, and $\omega = 2\pi f$ is the angular frequency.

B. Resonator

The resonator is a three-port passive RF geometry constituted of two coaxial transmission lines’ branches, as illustrated in Fig. 3. Port 1 is the input port of the geometry and is connected to the RF generator. Ports 2 and 3 are connected to two short circuits of variable lengths and resistance, adjusted to create an SW pattern. On the left of Fig. 3, the inner (bottom) and outer (top) conductors of the resonating loop are shown. Different colors refer to various materials: green for silver-coated conductors, light red for copper-coated conductors, and violet for stainless steel conductors.

Herein, the resonator’s frequency of interest is 63 MHz . Therefore, to minimize the reflected power back to the RF generator (S_{11} parameter at Port 1) at the frequency of interest, the physical length of the two variable-matching coaxial transmission lines connected to Ports 2 and 3 is optimized. To do it, we use ANSYS Electronics as shown in Fig. 4, where two resistors are added to Ports 2 and 3 to model the connected resistive shorts. Once the lengths minimizing the reflected power at Port 1 are determined, the electric field pattern in the resonator is similar to the plot on the right of Fig. 3, where it is seen that the wave is an SW consisting of a resultant from an incident and reflected waves.

To perform multipactor analysis for such configurations, we create numerous multipactor sections of homogeneous geometry and/or electric field, following the method described in [8]. For the resonator, 19 sections are chosen, whose location of each is indicated with numbered arrows in Fig. 3. Details on each section’s type and material are given in Table I.

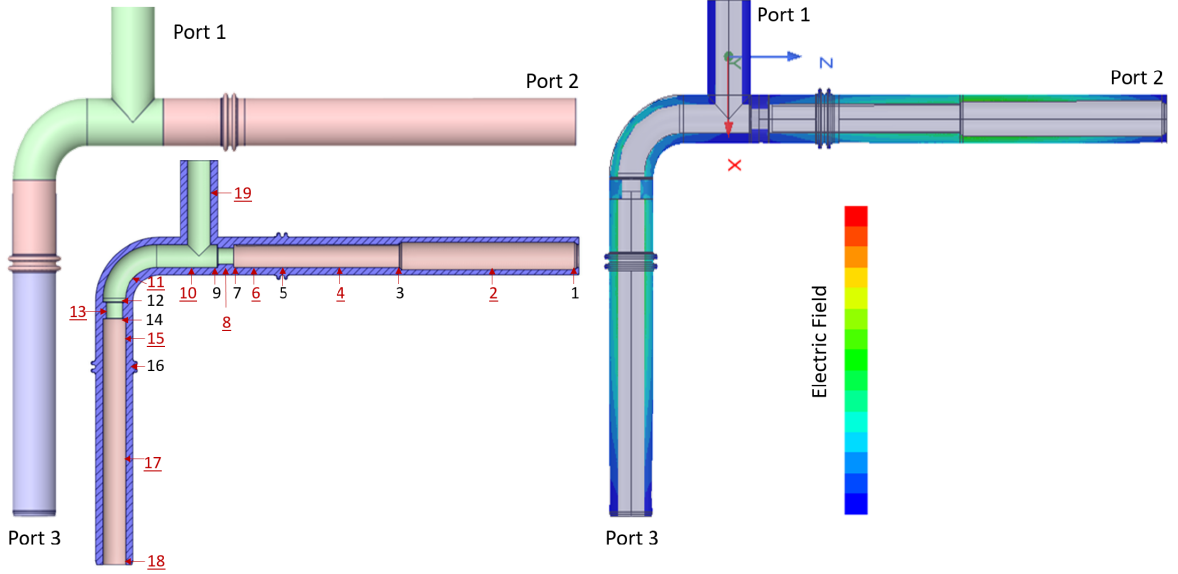


Fig. 3. Left: resonator inner (bottom) and outer (top) conductors materials. Green refers to silver, light red refers to copper, and light violet refers to stainless steel. The numbers refer to the different multipactor sections. The underlined red sections' number refers to the sections that are found to be prone to multipactor. Right: resonator's electric field plot, where the ports' excitation corresponds to the ones obtained from the circuit analysis, leading to an SW with a minimized reflected power on the RF generator port (Port 1).

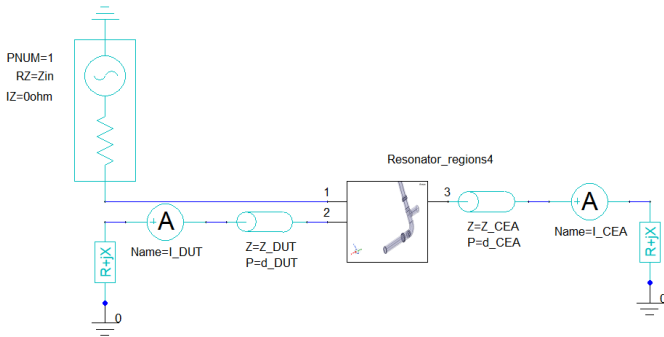


Fig. 4. Resonator circuit used to minimize the reflected power back to Port 1 at the frequency of interest, while the other two ports are short-circuited to create an SW pattern. The variable parameters are d_{DUT} and d_{CEA} being the physical length of the variable coax terminations.

IV. METHODOLOGY

To identify two multipactor thresholds for the ignition and extinction of the multipactor phenomenon, regardless of the value of the reflection coefficient, we investigate the case of a coaxial transmission line for its simplicity. Let us consider a coaxial transmission line, for which we suppose that the multipactor conditions are simultaneously fulfilled at a given frequency so that the multipactor voltage thresholds $V_{mp,lower}$ and $V_{mp,upper}$ are known [7], as represented in Fig. 5. The multipactor region, bounded by the red dashed lines of Fig. 5 being the lower ($V_{mp,lower}$) and upper ($V_{mp,upper}$) voltage multipactor thresholds, is constant regardless of the wave pattern and is dependent solely on the frequency, and geometry's dimensions and material.

The coaxial transmission line geometry will be subjected to different wave patterns for relevant physical quantities identification of the lower and upper multipactor thresholds and the multipactor location identification from ignition to extinction

phase. Fig. 5 represents different voltage magnitudes for different wave patterns as a function of the position along the wave propagation direction z of the coaxial transmission line represented in Fig. 1. Three wave patterns are considered.

- 1) TW, i.e., $R = 0$ illustrated in Fig. 5(a)–(c). The blue horizontal line represents the constant voltage V .
- 2) MW is illustrated in Fig. 5(d)–(f). The orange curve represents the voltage pattern of a coaxial transmission line subject to MW with $R = 0.5$ and $\psi = 0^\circ$ (the voltage SWR quantifying the reflected power is defined as $VSWR = (V_{max}/V_{min}) = (1 + R/1 - R) = 3$) so that the voltage's minimum is $(V(1 - R)/(1 + R^2))^{1/2}$ and the voltage maximum is $(V(1 + R)/(1 + R^2))^{1/2}$.
- 3) SW illustrated in Fig. 5(g)–(i). The green curve represents the voltage in a coaxial transmission line subject to an SW with $R = 1$ and $\psi = 0^\circ$ ($VSWR = \infty$) so that the voltage's minimum is zero, and the voltage's maximum is $(2)^{1/2}V$. V is progressively increased when going from Fig. 5(a) to (c), from Fig. 5(d) to (f), and from Fig. 5(g) to (i).

For the TW case, when $V < V_{mp,lower}$, no multipactor occurs. When $V_{mp,lower} \leq V \leq V_{mp,upper}$, the multipactor can take place along the coaxial transmission line, as represented in Fig. 5(a)–(c). For the MW and SW cases, we can observe that once the peaks of the orange and green curves reach the value $V_{mp,lower}$ [respectively, in Fig. 5(d) and (g)], the multipactor can take place in the vicinity of the maximal voltage location only. The latter reveals that the ignition of the multipactor is controlled by the peak voltage on the line (i.e., peak electric field), regardless of the wave pattern, and is localized in the vicinity of the maximal voltage. Moreover, for the MW and SW cases, once the multipactor region intersects the voltage pattern seen across the line [illustrated, respectively, in Fig. 5(e) and (h)], the multipactor will be triggered in

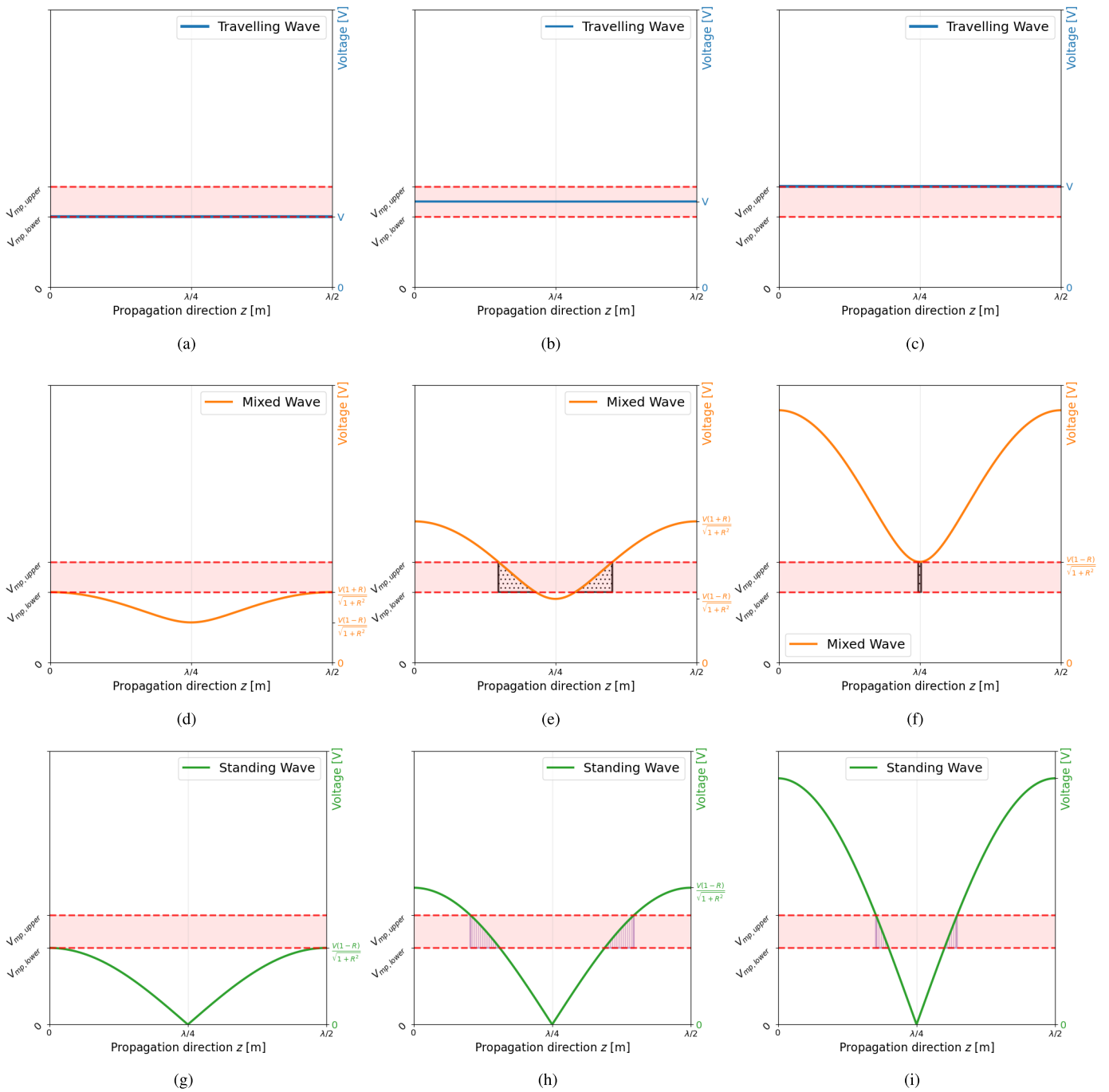


Fig. 5. Different multipactor phases for a given coaxial transmission line experiencing three different wave patterns—a traveling waveform: from (a) to (c); a mixed waveform: from (d) to (f); and a standing waveform: from (g) to (i). (a) Ignition multipactor phase along the structure. (b) Intermediate multipactor phase along the structure. (c) Extinction multipactor phase along the structure. (d) Ignition multipactor phase localized at the maximal voltage. (e) Intermediate multipactor phase drifting toward the minimal voltage region. (f) Extinction multipactor phase localized at the minimal voltage. (g) Ignition multipactor phase localized at the maximal voltage. (h) Intermediate multipactor phase drifting toward the minimal voltage region. (i) Theoretically, there is no multipactor extinction phase for SW pattern.

the zones where the voltage is within the multipactor region. These zones are represented as a dotted zone for the MW case and a hatched zone for the SW case and correspond to the geometry's parts where the multipactor conditions are simultaneously fulfilled. The latter reveals that for both MW and SW, as the voltage V increases, a displacement in the location of the sustained-multipactor phenomenon is observed, and therefore, the multipactor drifts from the maximal voltage's

vicinity toward the minimal voltage's location on the line. Moreover, one can remark that for such cases, the maximal voltage observed on the line is no more the relevant physical quantity, in terms of location and value, for the developed multipactor.

Theoretically, for the MW case, the multipactor extinction takes place when the minimal voltage across the line reaches a value higher than $V_{mp,upper}$, as illustrated in Fig. 5(f). Therefore,

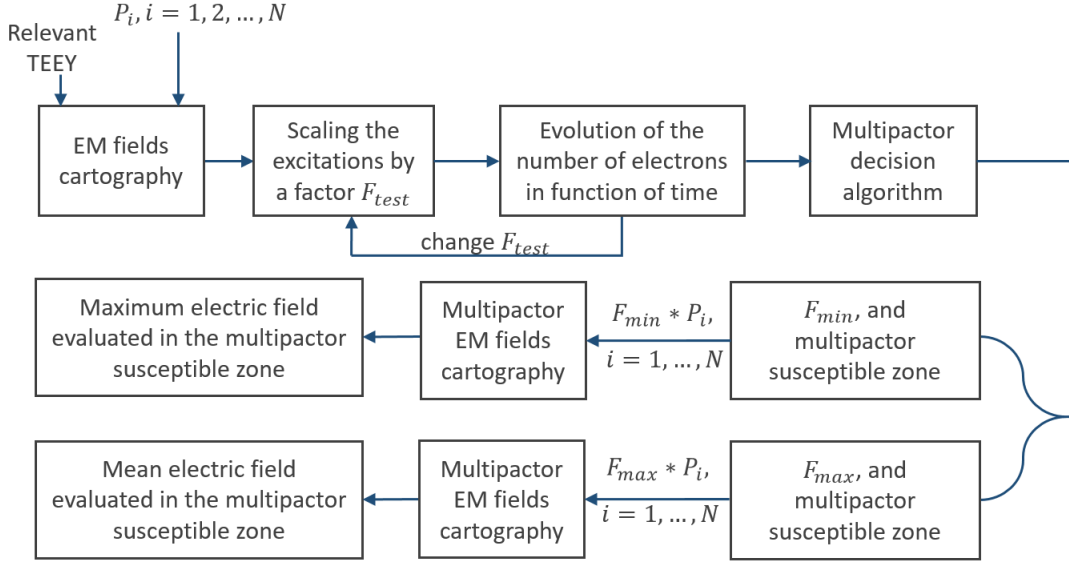


Fig. 6. Steps summarizing the applied methodology for the determination of the multipactor electric field thresholds, which are constant regardless of the SW ratio, for each defined multipactor region.

the multipactor is localized in the minimal voltage vicinity before extinction. Nevertheless, there is always a null voltage across the line for the pure SW case. The latter means that, theoretically, the multipactor could always be sustained close to the voltage nodes for SW. It should be noted that, in reality, due to the space charge effects [19], nonlinear effects, such as ponderomotive force [21], as well as the surface conditioning effects (reduction of TEEY) [7], the multipactor is no more sustained above a certain barrier, even for the pure SW case.

As for generic and multiport complex geometries, it is sometimes not possible to define a voltage unequivocally, and as the electric field is the gradient of the voltage ($\vec{E} = -\nabla V$), the multipactor thresholds are expressed as multipactor electric field thresholds rather than voltage thresholds.

Motivated by the coaxial transmission line analysis, we expect that the maximal multipactor electric field's magnitude of the multipactor-susceptible zone corresponds to the ignition of the multipactor and remains almost the same for the three wave patterns (TW, MW, or SW). Moreover, we expect that the mean (i.e., average) multipactor electric field's magnitude, calculated in the multipactor-susceptible zone, corresponds to the extinction of the multipactor and remains almost the same for the three wave patterns. The multipactor-susceptible zone corresponds to the geometry's part where the multipactor conditions are simultaneously fulfilled. We expect that this principle is also true when working with complex 3-D geometries, as will be shown in Section V-B.

A. Implementation

The software used for multipactor analysis is Spark-3D,¹ and the multipactor decision algorithm is detailed in [7]. As our software's version only supports a single TEEY, the

sections having multiple TEEY will be analyzed for each TEEY, composing the section separately.

For an imported geometry into Spark-3D, the total initial incident power on all the ports of the geometry must be equal to 1 W. If the imported geometry has one activated port, then the software will give, as output, the multipactor incident power(s). Otherwise, if the imported geometry has N -activated ports, where each port i has an initial incident power P_i , $i = 1, \dots, N$, such that the total initial incident power is one, i.e., $\sum_{i=1}^N P_i = 1$ W, the software's output is a scaling factor F , and once multiplied by each port's incident power (P_i), it gives the ports' incident powers triggering multipactor in the analyzed geometry. In other terms, to obtain the multipactor electric field in the geometry, each port will have an incident power equal to $P_i \times F$, $i = 1, \dots, N$. Note that if the geometry has two multipactor thresholds, then the output of the multipactor decision algorithm is two scaling factors F_{\min} and F_{\max} for the ignition and extinction of the multipactor, respectively. As we are dealing with coaxial transmission lines having two thresholds [7], we stick to F_{\min} and F_{\max} .

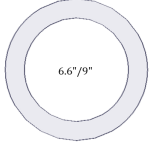
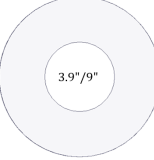
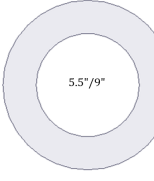
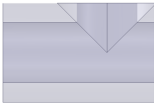

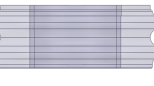


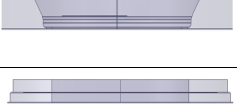
As varying the reflection coefficient can be obtained by changing the initial incident power on the different geometry's ports, the scaling factors F_{\min} and F_{\max} obtained by the multipactor software will vary as well. Therefore, for each port and each reflection coefficient, we associate an incident multipactor power, which is not practical, especially with multiport geometries of variable reflection coefficients. Therefore, defining the multipactor thresholds as electric field multipactor thresholds rather than multipactor incident power thresholds is crucial.

The proposed methodology will be implemented, as illustrated in Fig. 6. In the first step, the EM field cartography is calculated by an EM solver (here, ANSYS-HFSS). After choosing the initial power ports' excitation and the appropriate TEEY curve, the EM field is imported into the multipactor solver (here, Spark-3D). In the second step, the scaling factor

¹Version 1.6.3.

TABLE I

DIFFERENT MULTIPACTOR-ANALYSIS SECTIONS OF THE RESONATOR STRUCTURE. THE TYPE OF THE GEOMETRY, SECTION'S NAME, INNER AND OUTER CONDUCTORS' SURFACE MATERIAL, AND THE IN-PLANE VACUUM ILLUSTRATION ARE GIVEN

Geometry	Section(s)	Inner conductor	Outer conductor	Vacuum Illustration
$\sim 18.74 \Omega$ coaxial geometry	S2	Copper	Copper	
50Ω coaxial geometry	S8, and S13	Silver	Copper	
30Ω coaxial geometry	S4, S6, and S15 S17 S19	Copper Copper Silver	Copper Inox Silver	
Tee-junction 30Ω coaxial geometry	S10	Silver	Silver	
Bend 30Ω coaxial geometry	S11	Silver	Silver	
Helical (bellows) 30Ω coaxial geometry	S5, and S16	Copper	Copper	
Tapered geometry ($50 \Omega - 30 \Omega$)	S7 S12 S9 S14	Copper Silver Silver Copper	Copper Copper Silver Copper	
Tapered geometry ($30 \Omega - \sim 18.74 \Omega$)	S1 S3	Copper Copper	Copper Copper	
Tapered geometry ($30 \Omega - 26 \Omega$)	S18	Copper	Inox	

F_{test} is iteratively changed for decision-making on the existence of a multipactor based on the number of electrons' evolution in time [7]. The output of this step is the determination of F_{min} and F_{max} , as well as the multipactor-susceptible zones where the multipactor conditions are simultaneously fulfilled (detailed in the following). After that, the ports' excitation is scaled with the multipactor scaling factors to generate the multipactor EM field cartography. The final step is the evaluation of the maximum and mean electric fields—in their corresponding multipactor-susceptible zones—

respectively, as the lower and upper multipactor thresholds, following the methodology proposed in Section IV.

The multipactor-susceptible zone is the zone of the simulated region where multipactor takes place for the lower and upper multipactor thresholds and, therefore, where the multipactor conditions are fulfilled simultaneously. The multipactor-susceptible zone is determined by analyzing the statistical data generated by Spark-3D. In particular, the average TEEY and the average impact energy for each surface mesh in the model are interesting statistical quantities for

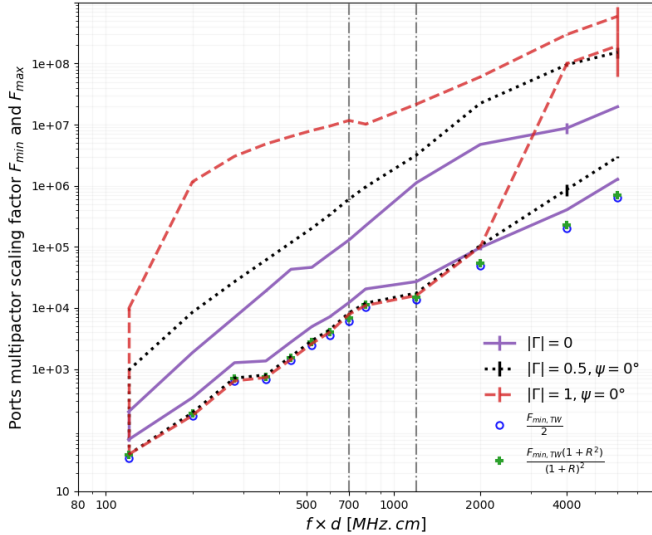


Fig. 7. Lower and upper multipactor scaling factors F_{\min} and F_{\max} , obtained by Spark-3D for the three wave patterns: TW, MW, and SW (detailed in Section III-A), are represented, respectively, in plain purple, black dotted, and red dashed. The green crosses and blue circles correspond to the scaling laws proposed by Somersalo et al. [6], respectively, for the MW case and the SW case.

defining the susceptible zone. The two conditions simultaneously imposed on a surface mesh to be considered in the multipactor-susceptible zone are the following: 1) the average TEEY of the surface mesh should be greater than or equal to one and 2) the average impact energy E_i should satisfy $E_{c,1} \leq E_i \leq E_{c,2}$, where $E_{c,1}$ and $E_{c,2}$ are, respectively, the first and second crossover energies of the TEEY imported data.

In the following, we are showing that the chosen relevant physical quantities for the ignition of the multipactor, the maximal electric field, and for its extinction, the mean electric field, are constant regardless of the initial chosen P_i , $i = 1, \dots, N$, and therefore regardless of the reflection coefficient up to some frequency.

V. RESULTS

A. Coaxial Transmission Line

First, we want to examine the scaling factors provided by the Spark-3D software for a 50- Ω coaxial transmission line to assess its variability with the reflection coefficient, i.e., its dependency on the ports' excitation. Fig. 7 represents the lower and upper scaling factors F_{\min} and F_{\max} obtained for the different wave patterns: TW (plain violet curve), MW (black dotted curve), and SW (dashed red curve) in the frequency range [25, 1500] MHz. Moreover, the scaling laws of Somersalo et al. [6], mentioned in Section II, for the MW and the SW cases as a function of the multipactor input power obtained for a TW case are represented, respectively, in blue circles and green crosses. The scaling laws are proposed for the lower multipactor thresholds.

In contrast to the findings of Perez et al. [9], where the 700-MHz \cdot cm barrier separates the regime of constant lower multipactor thresholds from the one with variable thresholds, our study reveals a distinct behavior. In our results, the first

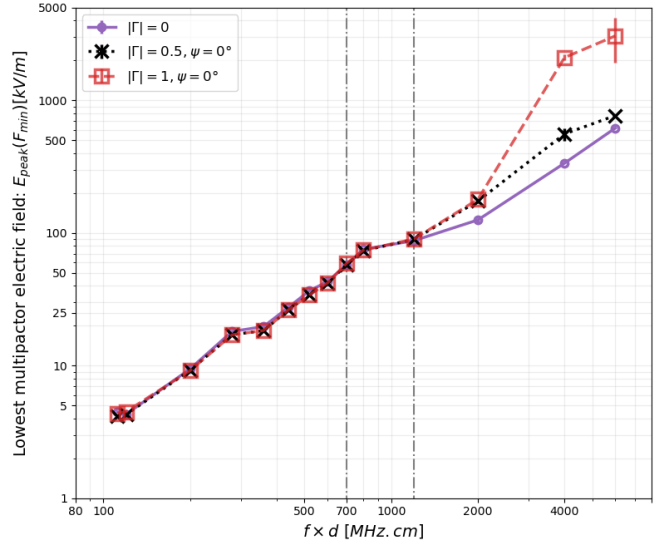


Fig. 8. Relevant physical quantity for the multipactor's ignition, which is the maximum electric field's magnitude evaluated in the multipactor-susceptible zone of the coaxial transmission line when the initial ports' excitation is scaled by the multipactor scaling factor F_{\min} . The lower multipactor electric field thresholds are evaluated for the three wave patterns detailed in Section III-A and are represented in plain purple, black dotted, and red dashed.

dashed-dotted gray vertical line denotes the 700-MHz \cdot cm barrier. This line signifies the boundary between the multipactor regime where the upper electric field multipactor thresholds remain constant, regardless of the variability of the reflection coefficient, and the regime where the electric field multipactor thresholds depend on the reflection coefficient. In addition, what distinguishes our study is the second critical point, represented by a barrier at 1200 MHz \cdot cm, surpassing the first one. Above this higher barrier, we observe the non-linear ponderomotive force's influence on the lower electric field multipactor thresholds. This discovery is motivated by our observation that the multipactor initiation occurs near the maximal electric field, where the ponderomotive force's magnitude is null. As the multipactor threshold increases, a displacement toward the electric field's node, correlated with an increase in the ponderomotive force, is observed. Therefore, intuitively, the effect of the ponderomotive force should be observed first for the upper and then the lower multipactor thresholds, as explained in detail in the Appendix.

Fig. 7 shows that the scaling factors F_{\min} and F_{\max} , corresponding to the ignition and extinction of multipactor, vary with the variability of the reflection coefficient. In addition to that, we remark that: 1) below the second barrier (at 1200 MHz \cdot cm), F_{\min} for the MW and SW cases (the lower branch, respectively, for the black dotted curve and the dashed red curve) shows a good agreement with the proposed scaling laws by Somersalo et al. [6] (respectively, the green crosses and the blue curves) and 2) above the second barrier, the proposed laws are no longer in good agreement with their corresponding simulated scaling factors. The latter is explained by the ponderomotive force's effect, as seen later.

Second, the methodology explained in Section IV-A is applied to the coaxial transmission line for the three wave

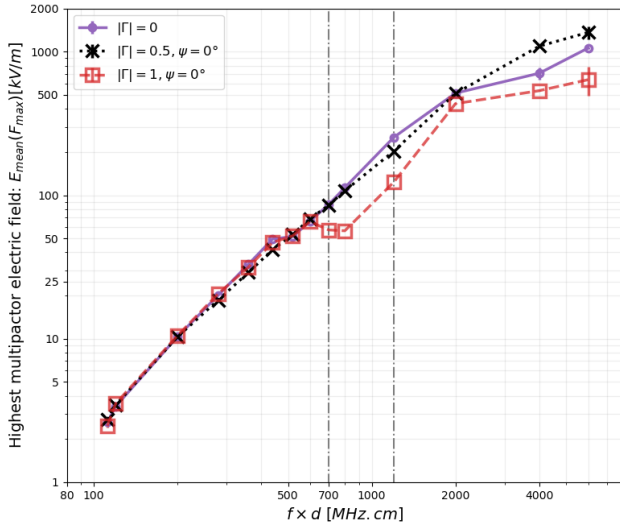


Fig. 9. Relevant physical quantity for the multipactor’s extinction, which is the mean electric field’s magnitude evaluated in the multipactor-susceptible zone of the coaxial transmission line when the initial ports’ excitation is scaled by the multipactor scaling factor F_{\max} . The upper multipactor electric field thresholds are evaluated for the three wave patterns detailed in Section III-A and are represented in plain purple, black dotted, and red dashed.

patterns to demonstrate the validity of the methodology below the first barrier at $700 \text{ MHz} \cdot \text{cm}$. Consequently, in this region of validity, the multipactor electric field thresholds remain constant regardless of the variability of the reflection coefficient.

The relevant physical quantity for the ignition (respectively, extinction) of multipactor, corresponding to the lower (respectively, upper) scaling factor F_{\min} (respectively, F_{\max}), for the TW, MW, and SW is represented in Fig. 8 (see Fig. 9).

Below $700 \text{ MHz} \cdot \text{cm}$ (respectively, $1200 \text{ MHz} \cdot \text{cm}$), the results show that the obtained upper (respectively, lower) electric field multipactor thresholds are constant for the different tested reflection coefficients, proving that the proposed methodology is valid below $700 \text{ MHz} \cdot \text{cm}$. The ponderomotive force does not affect the electron dynamics below $700 \text{ MHz} \cdot \text{cm}$.

Nevertheless, the nonlinearity effect of the ponderomotive force is more pronounced above $700 \text{ MHz} \cdot \text{cm}$ for the upper multipactor thresholds as indicated by the fact that the multipactor electric field responsible for the extinction of multipactor in the SW case is smaller than that of the TW case, as the multipactor extinction takes place easier when there is a significant force pushing the electrons toward the nodes of the electric field. Moreover, above $1200 \text{ MHz} \cdot \text{cm}$, it affects the lower multipactor thresholds, where we notice that the multipactor electric field responsible for the ignition of multipactor in the SW case is higher than that of the TW case, as more power is needed to trigger multipactor since the ponderomotive force is attracting the electrons toward the electric field nodes without having enough energy to maintain a multipactor in the nodes’ vicinity.

Our results agree with Perez et al. [9], except for having two nonlinearity-triggering barriers for the upper and then the lower multipactor thresholds. The nonlinearity-triggering

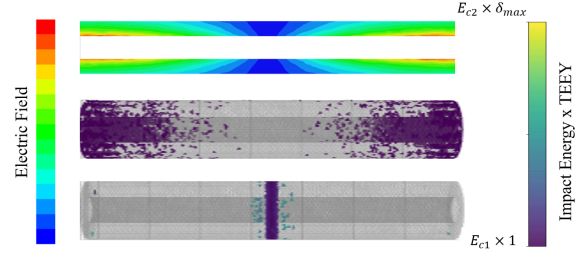


Fig. 10. Top: electric field representation (corresponding to the color map on the left) for an SW propagating in the coaxial transmission line. Middle (respectively, bottom): multipactor-susceptible zone located near the maximal (respectively, minimal) electric field for the lower (respectively, upper) multipactor threshold. The color map of the susceptible zones is represented on the right side.

$f \times d$ product for the upper multipactor thresholds is lower than that of the lower ones.

It should be noted that the results of Figs. 8 and 9 cannot be quantitatively compared as they refer to different quantities evaluated in different susceptible zones (Fig. 10).

Below $4000 \text{ MHz} \cdot \text{cm}$, the multipactor’s susceptible zone, for the lower (respectively, upper) multipactor thresholds, is in the vicinity of the maximal (respectively, minimal) electric field on the line as expected for the coaxial transmission line as represented in Fig. 10.

Nevertheless, above $4000 \text{ MHz} \cdot \text{cm}$, the ponderomotive force in the axial direction outperforms that in the radial direction over a wide range of the coaxial transmission line. The latter is due to the reduced distance between the maximum of the electric field and its node. As a result, electrons are pushed toward the direction of the electric field node before initiating any multipactor process. Subsequently, the ignition and extinction of the multipactor occur in the vicinity of the electric field’s nodes, as illustrated in Fig. 11. This observation could explain the minimal difference between the lower and upper multipactor scaling factors. In this scenario, the lower scaling factor tends to overlap with the upper scaling factor, triggering the multipactor in the geometry for the $f \times d$ products of 4000 and $6000 \text{ MHz} \cdot \text{cm}$ in the SW case, as seen in Fig. 7.

Consequently, our analysis elucidates the role of the ponderomotive force in influencing multipactor thresholds for a coaxial transmission line at different $f \times d$ products. Specifically, at low $f \times d$ products ($< 700 \text{ MHz} \cdot \text{cm}$), the radial component dominates, rendering the ponderomotive force negligible. At intermediate $f \times d$ products ($700 \text{ MHz} \cdot \text{cm} < f \times d < 1200 \text{ MHz} \cdot \text{cm}$), the axial ponderomotive force becomes significant near the field nodes, affecting only the upper multipactor threshold. However, at higher $f \times d$ products ($> 1200 \text{ MHz} \cdot \text{cm}$), the axial ponderomotive force becomes the dominant factor, impacting both upper and lower multipactor thresholds. Therefore, the methodology is valid below $< 700 \text{ MHz} \cdot \text{cm}$ for the coaxial transmission line of $50\text{-}\Omega$ characteristic impedance.

B. Resonator

In this section, the simulations aim to demonstrate the equivalence of multipactor electric field thresholds for the

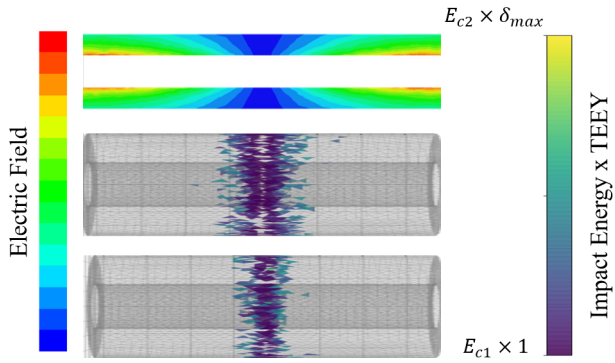


Fig. 11. Top: electric field representation (corresponding to the color map on the left) for an SW propagating in the coaxial transmission line, for an $f \times d$ product above $4000 \text{ MHz} \cdot \text{cm}$. Middle (respectively, bottom): multipactor-susceptible zone located near the minimal electric field for the lower (respectively, upper) multipactor threshold. The color map of the susceptible zones is represented on the right side.

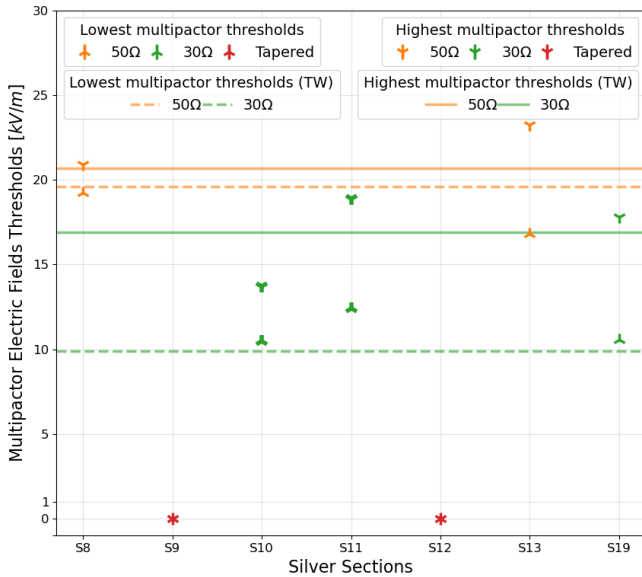


Fig. 12. Relevant physical quantities for the multipactor's ignition and extinction when the initial ports' excitation is scaled by the multipactor scaling factor F_{\min} and F_{\max} . The horizontal lines are the physical quantities obtained for a TW in coaxial transmission lines of different characteristic impedances. Silver material sections are considered.

SW pattern within the resonator to those in simplified coaxial transmission lines with TWs—assuming equal characteristic impedance. Specifically, we apply the developed methodology to determine the maximal (respectively, mean) multipactor electric field evaluated in the susceptible zone corresponding to the ignition (respectively, extinction) of multipactor in each resonator section. The analysis is performed for each material type separately. Sections with identical geometries and materials but different electric fields (as illustrated in Fig. 3) are considered comparable. Furthermore, the results for the coaxial transmission line sections are compared to the reference TW case results. Figs. 12–14 represent the lower and upper multipactor electric field thresholds obtained by our methodology for the silver, stainless steel, and copper material

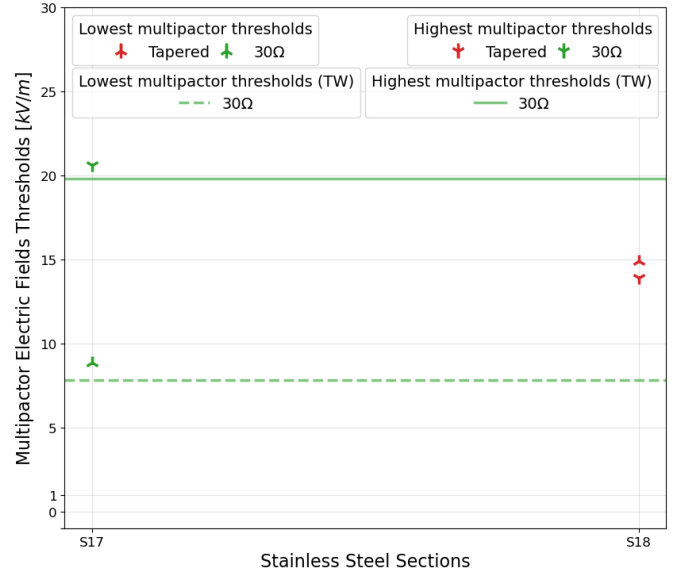


Fig. 13. Relevant physical quantities for the multipactor's ignition and extinction when the initial ports' excitation is scaled by the multipactor scaling factor F_{\min} and F_{\max} . The horizontal lines are the physical quantities obtained for a TW in coaxial transmission lines of different characteristic impedances. Stainless steel material sections are considered.

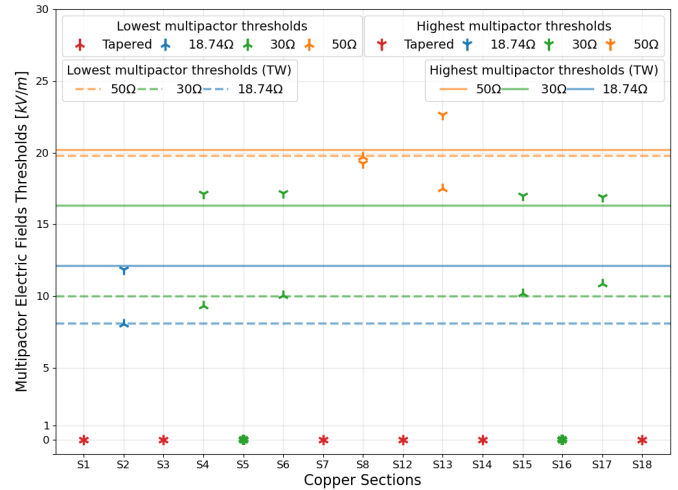


Fig. 14. Relevant physical quantities for the multipactor's ignition and extinction when the initial ports' excitation is scaled by the multipactor scaling factor F_{\min} and F_{\max} . The horizontal lines are the physical quantities obtained for a TW in coaxial transmission lines of different characteristic impedances. Copper material sections are considered.

sections, respectively. Each point on the figures represents the averaged result obtained from three simulation runs.

As represented in Fig. 12, the silver-coated tapered geometries S9 and S12 are not prone to multipactor (red markers). The lower and upper electric field multipactor thresholds of 50-Ω coaxial transmission line geometries S8 and S13 (orange markers) are within at maximum 15% of the ones obtained for the same geometry subject to TW (orange plain and dashed horizontal lines). The same is observed for the 30-Ω coaxial transmission line S19 (green). The electric field thresholds of S10 and S11 are represented as bold green markers since the geometries are not typical 30-Ω coaxial transmission lines, yet

their thresholds are comparable to the ones of a typical 30- Ω coaxial transmission line.

Similarly, as illustrated in Fig. 14, the copper-coated tapered geometries (S1, S3, S7, S12, S14, and S18) are not prone to multipactor. The lower and upper electric field multipactor thresholds for the 18.74- Ω (S2), 30- Ω (S4, S6, S15, and S17), and 50- Ω (S8 and S13) coaxial transmission lines are at most within 15% of the multipactor thresholds obtained for the same geometry subject to a TW pattern. The outer conductor bellows 30- Ω (S5 and S16) are not prone to multipactor (bold green markers).

The same conclusion is applied to the stainless steel 30- Ω coaxial transmission line (S17), as shown in Fig. 13. It was found that the stainless steel material tapered geometry S18 is prone to multipactor, and its multipactor thresholds are determined.

These results show that our methodology is also valid for the resonator's complex structure operating at 63 MHz as the multipactor of the sections having the same geometries is almost similar regardless of the wave pattern. Once the multipactor conditions are met for the analyzed sections, the ignition (extinction) of the multipactor is in the vicinity of the high (low) electric field magnitude seen on the section. The sections prone to multipactor are marked with underlined red numbers in Fig. 3.

VI. CONCLUSION

We introduced a novel methodology for characterizing multipactor thresholds, focusing on the ignition and extinction of multipactor phenomena across various wave patterns and reflection coefficients. Our approach relies on evaluating the maximum and mean electric field magnitudes in the multipactor-susceptible zones, providing a unified framework for understanding lower and upper multipactor thresholds, irrespective of underlying wave patterns or reflection coefficients. The developed methodology was found to be valid in a region before the dominance of the ponderomotive force's nonlinear effects.

Our findings revealed that, regardless of the complexity of geometries and the number of ports, the lower multipactor threshold crucially depends on the maximum electric field and the upper multipactor threshold depends on the mean electric field. This insight establishes a foundation for predicting multipactor thresholds in scenarios with varying wave ports' excitation.

We validated our methodology through extensive simulations, focusing on a 50- Ω coaxial transmission line and a complex three-port resonating geometry. The results demonstrate the robustness of our approach, particularly in frequency regimes below 700 MHz \cdot cm for the coaxial transmission line. Furthermore, the methodology is valid across the geometries of the resonator structure by comparing multipactor thresholds obtained with an SW pattern to those of a TW pattern for a coaxial transmission line with similar characteristic impedance.

Therefore, the methodology is applicable to predict multipactor thresholds in diverse EM systems where the reflection coefficient is variable, such as the ICRH antennas of the

experimental tokamak WEST, operating in the frequency range [46, 65] MHz and subject to wave patterns of variable reflection coefficients.

In conclusion, this work contributes to a nuanced understanding of multipactor thresholds and presents a robust methodology applicable to varied scenarios with complex geometries and various frequencies.

APPENDIX

From the expression of the ponderomotive force, it is seen that this force has a component in the radial direction due to the nonhomogeneity of the electric field in a coaxial transmission line and an axial component that only exists if the electric field is nonhomogeneous in the wave propagation direction z . Therefore, the axial component of the ponderomotive force is nonzero in the case of an MW or an SW.

We exploit herein the case of an SW, where the electric field can be expressed by simple trigonometric identities applied on (1) as

$$\vec{E}(\vec{r}, t) = \frac{\sqrt{2}V}{r \ln\left(\frac{b}{a}\right)} \cos(\omega t) \cos(\beta z) \vec{e}_r = \vec{E}_S(\vec{r}) \cos(\omega t)$$

where $\vec{E}_S(\vec{r})$ is the spatial vector of the electric field.

From the derivation of the ponderomotive force [21], we can find that the radial and axial components are expressed by

$$\vec{F}_r = \frac{q^2}{m\omega^2} \frac{|\vec{E}_S|^2}{r} \vec{e}_r, \quad (3)$$

$$\vec{F}_z = \frac{q^2}{m\omega^2} |\vec{E}_S|^2 \frac{\beta \sin(\beta z)}{\cos(\beta z)} \vec{e}_z. \quad (4)$$

Figs. 15–18 represent the average radial and axial components of the ponderomotive force averaged over one time period corresponding to the upper multipactor threshold of the coaxial transmission line at the $f \times d$ products. The ponderomotive force only affects the multipactor threshold if $|\vec{F}_z| > |\vec{F}_r|$ in the region where the multipactor is triggered (i.e., $V_{\text{mp,lower}} \leq V \leq V_{\text{mp,upper}}$).

Here is an explanation for each $f \times d$ product.

- 1) 120 MHz \cdot cm: An $f \times d$ for which the proposed methodology is valid as the radial component is always greater than the axial component.
- 2) 700 MHz \cdot cm: An $f \times d$ barrier above which the proposed methodology is nonvalid for the upper multipactor threshold as the axial component outperforms the radial component near the center of the coaxial transmission line where the electric field node is located—multipactor-susceptible zone of the upper multipactor threshold.
- 3) 1200 MHz \cdot cm: An $f \times d$ barrier above which the proposed methodology is nonvalid for the lower multipactor threshold as the axial component of the ponderomotive force becomes dominant over a larger segment of the coaxial transmission line and the electric field peak and node are becoming closer to each other.
- 4) 4000 MHz \cdot cm: An $f \times d$ for which the proposed methodology is nonvalid for the lower and the upper multipactor threshold.

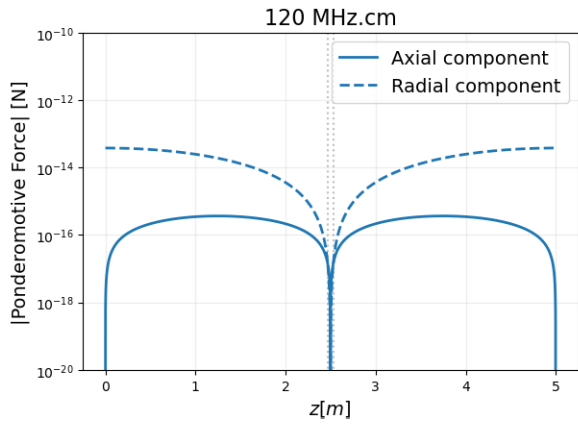


Fig. 15. Magnitude of the axial and radial components of the ponderomotive force versus the wave propagation direction z . The plots correspond to the upper multipactor threshold but have the same shape for the lower multipactor threshold with slightly lower values and therefore are omitted. The plots correspond to $120 \text{ MHz} \cdot \text{cm}$.

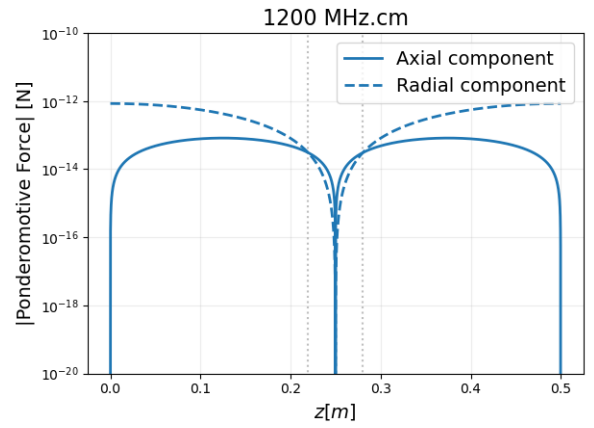


Fig. 17. Magnitude of the axial and radial components of the ponderomotive force versus the wave propagation direction z . The plots correspond to the upper multipactor threshold but have the same shape for the lower multipactor threshold with slightly lower values and therefore are omitted. The plots correspond to $1200 \text{ MHz} \cdot \text{cm}$.

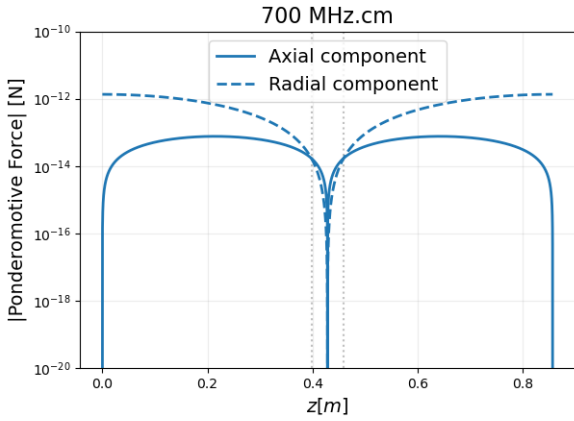


Fig. 16. Magnitude of the axial and radial components of the ponderomotive force versus the wave propagation direction z . The plots correspond to the upper multipactor threshold but have the same shape for the lower multipactor threshold with slightly lower values and therefore are omitted. The plots correspond to $700 \text{ MHz} \cdot \text{cm}$.

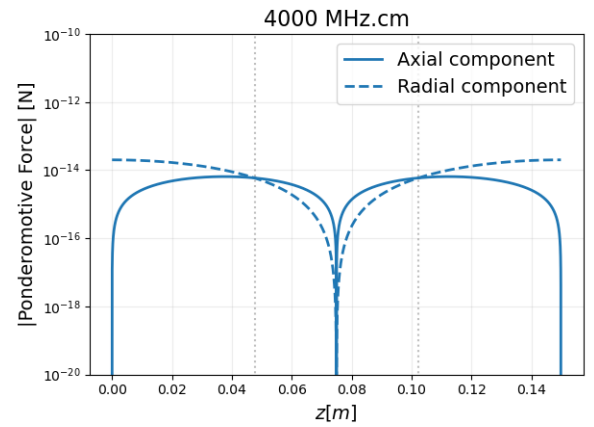


Fig. 18. Magnitude of the axial and radial components of the ponderomotive force versus the wave propagation direction z . The plots correspond to the upper multipactor threshold but have the same shape for the lower multipactor threshold with slightly lower values and therefore are omitted. The plots correspond to $4000 \text{ MHz} \cdot \text{cm}$.

For the lower multipactor thresholds, the two components of the ponderomotive force have the same shape but different values and are not plotted for clarity purposes.

At $120 \text{ MHz} \cdot \text{cm}$, the radial component's magnitude is higher than that of the axial component, i.e., the force pushing the electrons toward the node of the electric field is negligible with respect to its radial counterpart. Hence, there is no effect for this nonlinear force at such low frequencies, and the proposed methodology is valid.

At $700 \text{ MHz} \cdot \text{cm}$, the radial component's magnitude is larger than that of the axial component, except for the region in the vicinity of the electric field node ($\sim 7\%$ of the coaxial transmission line). Hence, the effect of this nonlinear force is more pronounced on the upper multipactor threshold but still insufficient for affecting the lower multipactor threshold, for which the multipactor is triggered near the maximal electric field. At higher $f \times d$, we observe that the region over which the axial component exceeds the radial one is wider ($\sim 12\%$ of the coaxial transmission line at $1200 \text{ MHz} \cdot \text{cm}$ and $\sim 36\%$ of the coaxial transmission line at $4000 \text{ MHz} \cdot \text{cm}$). Therefore,

the nonlinear effect will be seen on the lower and upper multipactor thresholds.

In summary, our analysis of the ponderomotive force components reveals a nuanced frequency-dependent behavior that plays a pivotal role in influencing multipactor thresholds at different locations along the coaxial transmission line. Notably, the dominance of the axial component becomes increasingly pronounced at higher frequencies, leading to a sequential impact on the upper and lower multipactor thresholds.

Importantly, our findings indicate that the nonlinearity-triggering $f \times d$ product for the upper multipactor thresholds is lower than that for the lower multipactor thresholds. This intriguing observation is attributed to the heightened influence of the axial component near the electric field nodes, particularly in regions closer to the center of the coaxial transmission line where the multipactor diminishes. As the $f \times d$ product increases, the axial component's effect progressively extends to regions with varying electric field characteristics, ultimately affecting the lower multipactor thresholds.

ACKNOWLEDGMENT

Views and opinions expressed are, however, those of the author(s) only and do not necessarily reflect those of the European Union or the European Commission. Neither the European Union nor the European Commission can be held responsible for them.

REFERENCES

- [1] J. M. Bernard et al., “New high power CW test facilities for ITER ICRH components testing,” *Fusion Eng. Design*, vol. 86, nos. 6–8, pp. 876–879, Oct. 2011, doi: [10.1016/j.fusengdes.2011.02.100](https://doi.org/10.1016/j.fusengdes.2011.02.100).
- [2] R. A. Kishkek, Y. Y. Lau, L. K. Ang, A. Valfells, and R. M. Gilgenbach, “Multipactor discharge on metals and dielectrics: Historical review and recent theories,” *Phys. Plasmas*, vol. 5, no. 5, pp. 2120–2126, May 1998, doi: [10.1063/1.872883](https://doi.org/10.1063/1.872883).
- [3] R. Woo, “Final report on RF voltage breakdown in coaxial transmission lines,” NASA, National Aeronautics and Space Administration, Washington, DC, USA, Tech. Rep. 32-1500, Oct. 1970. [Online]. Available: <https://ntrs.nasa.gov/archive/nasa/casi.ntrs.nasa.gov/19700033786.pdf>
- [4] J. R. M. Vaughan, “Multipactor,” *IEEE Trans. Electron Devices*, vol. ED-35, no. 7, pp. 1172–1180, Jul. 1988, doi: [10.1109/16.3387](https://doi.org/10.1109/16.3387).
- [5] T. P. Graves, S. J. Wukitch, B. LaBombard, and I. H. Hutchinson, “Effect of multipactor discharge on Alcator C-mod ion cyclotron range of frequency heating,” *J. Vac. Sci. Technol. A, Vac., Surf., Films*, vol. 24, no. 3, pp. 512–516, May 2006, doi: [10.1116/1.2194937](https://doi.org/10.1116/1.2194937).
- [6] E. Somersalo, P. Yla-Oijala, D. Proch, and J. Sarvas, “Computational methods for analyzing electron multipacting in RF structures,” *Part. Accel.*, vol. 59, pp. 107–141, Jan. 1998.
- [7] E. Al Hajj Sleiman, J. Hillairet, M. Belhaj, and S. Dadouch, “Evaluation of multipactor thresholds for coaxial lines subject to surface conditioning for the WEST ion cyclotron antenna,” *Fusion Eng. Design*, vol. 185, Dec. 2022, Art. no. 113325, doi: [10.1016/j.fusengdes.2022.113325](https://doi.org/10.1016/j.fusengdes.2022.113325).
- [8] E. A. H. Sleiman, J. Hillairet, and M. Belhaj, “Multipactor-triggering powers’ modelling of a WEST ICRH antenna during RF conditioning,” *IEEE Trans. Plasma Sci.*, vol. 51, no. 5, pp. 1247–1255, May 2023, doi: [10.1109/TPS.2023.3268293](https://doi.org/10.1109/TPS.2023.3268293).
- [9] A. M. Perez et al., “Prediction of multipactor breakdown thresholds in coaxial transmission lines for traveling, standing, and mixed waves,” *IEEE Trans. Plasma Sci.*, vol. 37, no. 10, pp. 2031–2040, Oct. 2009, doi: [10.1109/TPS.2009.2028428](https://doi.org/10.1109/TPS.2009.2028428).
- [10] G. Romanov, “Stochastic features of multipactor in coaxial waveguides for travelling and standing waves,” Fermi Nat. Accel. Lab. (FNAL), Batavia, IL, USA, Tech. Rep. ERMILAB-PUB-11-003-TD, Feb. 2011.
- [11] J. Hillairet, “RF network analysis of the WEST ICRH antenna with the open-source Python scikit-RF package,” in *Proc. AIP Conf.*, vol. 2254, Sep. 2020, Art. no. 070010, doi: [10.1063/5.0013523](https://doi.org/10.1063/5.0013523).
- [12] E. W. B. Gill and A. von Engel, “Starting potentials of high-frequency gas discharges at low pressure,” *Proc. Roy. Soc. London, A, Math. Phys. Sci.*, vol. 192, no. 1030, pp. 446–463, Feb. 1948, doi: [10.1098/rspa.1948.0018](https://doi.org/10.1098/rspa.1948.0018).
- [13] J. de Lara et al., “Multipactor prediction for on-board spacecraft RF equipment with the MEST software tool,” *IEEE Trans. Plasma Sci.*, vol. 34, no. 2, pp. 476–484, Apr. 2006, doi: [10.1109/TPS.2006.872450](https://doi.org/10.1109/TPS.2006.872450).
- [14] V. Petit, M. Taborelli, H. Neupert, P. Chiggiato, and M. Belhaj, “Role of the different chemical components in the conditioning process of air exposed copper surfaces,” *Phys. Rev. Accel. Beams*, vol. 22, no. 8, Aug. 2019, Art. no. 083101, doi: [10.1103/physrevaccelbeams.22.083101](https://doi.org/10.1103/physrevaccelbeams.22.083101).
- [15] J. Hillairet et al., “Multipactor in high power radio-frequency systems for nuclear fusion,” in *Proc. MULCOPIM*, Apr. 2017. [Online]. Available: <https://hal-cea.archives-ouvertes.fr/cea-01612959>
- [16] A. Sounas, “Modeling of long-term multipactor evolution in microwave components including dielectric layers,” Ph.D. dissertation, Fac. Sci. Technol., Lab. ElectroMagn. Acoust. (LEMA), EPFL, Lausanne, Switzerland, 2015. [Online]. Available: <http://infoscience.epfl.ch/record/206111>
- [17] F. Höhn, W. Jacob, R. Beckmann, and R. Wilhelm, “The transition of a multipactor to a low-pressure gas discharge,” *Phys. Plasmas*, vol. 4, no. 4, pp. 940–944, 1997, doi: [10.1063/1.872564](https://doi.org/10.1063/1.872564).
- [18] J. Hillairet et al., “R&D activities on RF contacts for the ITER ion cyclotron resonance heating launcher,” *Fusion Eng. Des.*, vols. 96–97, pp. 477–481, Apr. 2015, doi: [10.1016/j.fusengdes.2015.04.005](https://doi.org/10.1016/j.fusengdes.2015.04.005).
- [19] E. Sorolla, A. Sounas, and M. Mattes, “Space charge effects for multipactor in coaxial lines,” *Phys. Plasmas*, vol. 22, no. 3, Mar. 2015, Art. no. 033512, doi: [10.1063/1.4915130](https://doi.org/10.1063/1.4915130).
- [20] M. Belhaj and S. Dadouch, “A simple method for energy calibration of keV incident electron beam using a contactless electrostatic voltmeter probe,” *Rev. Sci. Instrum.*, vol. 92, no. 8, Aug. 2021, Art. no. 083301, doi: [10.1063/5.0057488](https://doi.org/10.1063/5.0057488).
- [21] F. Chen, *Introduction to Plasma Physics and Controlled Fusion*, 3rd ed. Cham, Switzerland: Springer, Jul. 2016, pp. 284–285, doi: [10.1007/978-3-319-22309-4](https://doi.org/10.1007/978-3-319-22309-4).